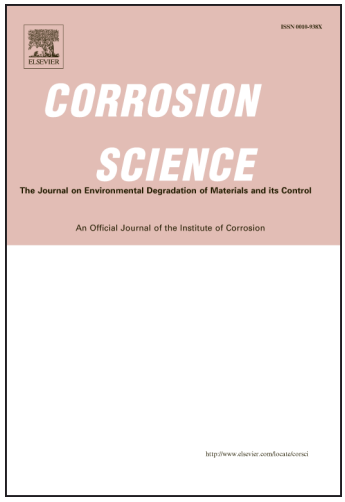

In-situ pH responsive fluorescent probing of localized iron corrosion

Xinjie Liu, Hugh Spikes, Janet S.S. Wong

PII: S0010-938X(14)00272-8
DOI: http://dx.doi.org/10.1016/j.corsci.2014.06.016
Reference: CS 5887

To appear in: *Corrosion Science*

Received Date: 24 March 2014
Accepted Date: 4 June 2014

Please cite this article as: X. Liu, H. Spikes, J.S.S. Wong, In-situ pH responsive fluorescent probing of localized iron corrosion, *Corrosion Science* (2014), doi: http://dx.doi.org/10.1016/j.corsci.2014.06.016

In-situ pH responsive fluorescent probing of localized iron corrosion

Xinjie Liu[1], Hugh Spikes[1] and Janet S. S. Wong[1]

[1]The Department of Mechanical Engineering, Imperial College London, London SW7 2AZ, UK

Correspondence to: Janet Wong (E-mail: *j.wong@imperial.ac.uk*)

Abstract

A fast and versatile method has been demonstrated to detect the early stage of iron corrosion *in-situ,* with minimum external perturbation, by using a pH sensitive fluorescence dye. The decreasing fluorescence intensity inside corrosion pits induced by hydrogen ions produced during iron corrosion is used as a signal indicator. Identification of corrosion pits (with resolution of < 1 μm) and quantification of corrosion rate based on local hydrogen concentration were achieved. The developed technique has been applied to show that surface roughness, under a constant current condition, influences the corrosion of iron. Corrosion occurs preferentially adjacent to local topographic features.

1 Introduction

Corrosion in aqueous environments is a commonly-encountered challenge when using metallic components. It is an electrochemical process that occurs at the solid-liquid interface and can lead to the dissolution of metal during the process of service. Components in oxidative and wet atmospheres, salt solutions, acids and alkalis are particular susceptible to corrosion. In the case of machines with moving parts such as gears and bearings, the rubbing together of surfaces promotes fretting, crevice corrosion and stress corrosion cracking. If left unmanaged, corrosion can lead to serious consequences including considerable economic costs due to production downtime and replacement, as well as health and safety problems.

While corrosion is eventually observed as rust, pit formation or weight loss, associated damage mechanisms such as fretting and crack formation, can occur at a very much earlier stage, long before corrosion sites are detectable by eye. Hence the detection, inhibition and ideally prevention of corrosion of metallic engineering materials at its earliest stages are essential to avoid critical engineering failures. A corrosion detection system able to detect corrosion at its infancy would thus be of great value in controlling engineering failures. It would also, by detecting and measuring the initial stages of corrosion, provide a means of testing the effectiveness of strategies for preventing corrosion, such as coatings and inhibitors over a reasonably short test time, without the present need for heavily accelerated tests involving the addition of salts, acids and other corrosion-enhancers with dubious validity to real systems.

Metal corrosion in aqueous environment involves the transfer of electrons between a metal surface and ions in an aqueous solution, usually in the presence of oxygen. Surface potential, in the form of electron work function (EWF), governs surface chemical reactivity and is very sensitive to the media or environment in which the surface is located. Any changes to the metal surface structure or chemical characteristics of the metal-liquid interface, such as mechanical strain [1,2], surface roughness (defect points) [3–5], existence of oxide layers [4], and adsorbed layers will alter EWF [1,6], and thus have significance to metal corrosion. Different fabrication and machining processes produce characteristic surface topographies and residual stress distributions in components. Hence corrosion on metal surfaces is often heterogeneous. However the effect of surface roughness on corrosion is controversial. Some researchers have suggested that pitting potential of stainless steel is lower for rougher surfaces than for the smoother ones [7–9] and that smoother surface finish reduces the incidence of growth of metastable pitting activity [10]. Kim *et al.* have reported that the corrosion rate of carbon steel increases with the surface roughness [11] while Li *et al.* also found that the EWF fluctuation of copper increases with an increase in roughness which may promote the formation of corrosion cell [5].

Also Abosrra *et al.* reported that, as the surface roughness of 316L stainless steel increased, the breakdown potential, the free corrosion potential and the width of passivity decreased, hence leading to an increase in corrosion rate [12]. However, in the case of mild steel specimens, it has been shown that improving surface finish leads to an increase in corrosion rate [12]. Other studies have found the effect of surface roughness is marginal compared to effect of residual stress [13,14]. It should be noted that none of the studies mentioned above examined initial stage corrosion, so it is not known whether surface roughness affects various stages of corrosion equally. To obtain a complete picture of the influence of surface features on metal corrosion, it is necessary to investigate corrosion of metal at its initiation.

To investigate the effect of surface roughness on metal corrosion, a technique sensitive to localised corrosion is needed. Localized corrosion has been studied for many metal alloys, where it has been found that chemical or physical heterogeneity at the surface, such as inclusions, second phase particles, flaws, mechanical damage, or dislocations are preferentially corroded [15]. Several detection methods, including electrochemical noise detection [16,17], magnetic flux leakage [18], acoustic emission technique [19], and scanning electrochemical microscopy (SECM) [20,21] have been applied. However, these techniques are either *ex-situ* methods or no local information can be obtained. *In situ* techniques, including near-field scanning optical microscopy (NSOM) [22], confocal laser scanning microscopy (CLSM) [23] and atomic force microscopy (AFM) [24-27] have been used to observe localized corrosion. However, none of them gives real time information of the progress of corrosion. Measurements were taken at least five minutes [25] or even one hour [27] after the test initiated. Hence information on incipient corrosion was lost.

Fluorescence imaging [22,24,25,28] (FI), which is capable of revealing the nature of the surface chemistry along with surface topography around the active sites, has proved particularly useful for real-time monitoring corrosion and interfacial chemical changes at solid electrodes [29] and solid-liquid interface [30,31]. Studies have mainly employed either fluorescent dye added in the solution itself or non-fluorescent

agents in the solution that form fluorescers and emit fluorescence after electrochemical reaction at interfaces. pH sensitive dyes were often used. Most studies have examined aluminium alloys [22,24,25,30,32] and rarely iron and steel which are more widely used in engineering. pH sensitive imaging fibre which involves coating an optical fibre with pH sensitive probes has been used to examine corrosion of 304 stainless steel wire [33]. In this study, corrosion of stainless steel was accelerated by immersing the sample in 0.1M KCl solution for 60 min followed by the application of 0.5 V bias for one minute. Rather large pits of two sizes: diameters of 12~20 μm and ~7 μm were revealed. The nature of the experiments in [33] means the technique is not sensitive to early stage corrosion and any sign of corrosion may have been developed for quite some time. Furthermore, 5 mM phosphate buffer (pH~6) was added in the corrosion media, which may accelerate corrosion and affect pH measurements [33]. Augustyniak and Ming [34] have incorporated specially synthesized pH sensitive probes, FD1, into epoxy coating, which were then applied to aluminium alloy samples. The corrosion of epoxy coated sample was examined after more than two days exposure to 3.5wt% NaCl solution by shining a handheld UV lamp on the sample. Areas where corrosion had occurred exhibited bright orange fluorescence. The rationale of the application of the probe-embedded coating was twofold. Firstly, it ensured that observations were only confined to the sample surfaces. In addition, it also emulated a commonly-encountered engineering situation where metal is covered with protective coating. However, this method cannot be applied to conditions where surfaces are generally not protected since the application of coating may result in corrosion mechanisms that are not representative of such conditions. In addition, if a different coating is needed, for example to promote coating adhesion, a different dye would have to be chosen and dye selection is non-trivial. These shortcomings considerably limited the usefulness of the technique. Some other reports based on pH sensitive probes have been qualitative and in general with quite low resolution [23,32]. The best temporal resolution achieved is about 5 minutes [30].

In the present study, hydrogen ions produced by localized corrosion on an iron surface is monitored *in-situ* by using a fluorescent dye, 5,6-caboxyl fluorescein (56CF), whose fluorescence intensity is pH sensitive. By using epi-fluorescence imaging, acidic corrosion pits generated on iron surface in an electrolyte solution can be mapped, and the real-time, localized pH changes can be quantified by measuring the localised fluorescence intensity at the pits. The method has sub-micron resolution, which makes it possible to monitor the very initial stage of corrosion process.

2. Materials and Methods

The corrosion of iron in salt solutions was monitored with epi-fluorescence imaging. This was implemented by dissolving 5,6-carboxyl fluorescein (56CF), a pH-sensitive fluorescent dye, in salt solution. When excited by an appropriate wavelength of light, its emission intensity varies with the pH of its surroundings. Thus local changes in pH can be monitored in order to detect, map and quantify incipient corrosion.

2.1 Sample Preparation and General Characteristics of the Material System

Iron rods (99.99%) of diameter 10 mm were purchased from Goodfellow UK and cut into discs. These were ground to create flat surfaces using three grades of abrasive paper, 400 grit, 800 grit and 4000 grit (MetPrep Ltd. UK). The root mean square, surface roughness, *Ra*, after grinding was measured using a Vecco NT9100 system with a 20× objective and was found to average 505.8±53.8 nm, 266.3±13.7 nm and 30.5±7.9 nm for the three grades of paper respectively. These iron surfaces will be addressed as *rough*, *medium* and *smooth* surfaces respectively in this work.

Chemicals were analytical grade and were employed as received. Deionised water with a minimum resistivity of 18.1 MΩcm was used for solution preparation. 0.1 M NaCl aqueous solution containing 50 μM dissolved 5,6-caboxyl fluorescein (Sigma Aldrich) was used as the corrosion medium. The pH of the freshly prepared corrosion solution was measured to be 4.60 using a Thermo Scientific VSTAR22 system.

The relationship between the emission intensity of 56CF and pH of a solution was quantified. Buffer solutions containing 10 μM 56CF and having pH values ranging from 2.20 to 8.00 were prepared using 0.2 M disodium hydrogen phosphate and 0.1 M citric acid solutions and their absorption and emission spectra were measured. The absorption and emission spectra of 10 μM 56CF in pH 7.00 buffer are shown in Figure 1a. The absorption and emission peaks are at 490 nm and 517 nm respectively. The effect of pH on the emission spectra of 10 μM 56CF is shown in Figure 1b. The fluorescence intensity of 56CF increases as pH of buffer rises from 2.20 (acidic) to 8.00 (basic). The sensitivity of 56CF to pH stems from its ability to chelate with both acidic ions and basic ions in the solution to produce different fluorescent complexes. The integrated intensity, I, is obtained by integrating the emission spectra between wavelengths 495 nm and 750 nm. As presented in Figures 1c, I increases monotonically with increasing pH and it plateaus when pH < 2 and pH > 7. Hence, 56CF is most sensitive as a pH indicator when local pH is between 2 and 7. The addition of NaCl does not change the emission intensity of 56CF. While the emission intensity of 56 CF is slightly temperature sensitive [35], the maximum temperature rise during experiments is estimated to be less than 2 K. Hence the effect of temperature is neglected. The negligible effect of temperature on fluorescence emission of 56CF is confirmed by the constant background intensity noted throughout the experiments.

As the corrosion solution has a pH of 4.60, the normalised intensity, I_N, is defined by I at a particular pH divided by I at pH = 4.60. The value of I_N over the range pH = 4.60 to pH = 2.20 is shown in Figure 1d. Figure 1d allows the pH of the solution to be obtained from I_N, *i.e.* the ratio measured I to the intensity prior to any corrosion.

2.2 Methodology

This study takes advantage of the sensitivity of 56CF emission to local pH and uses it to identify local corrosion sites. The possible reactions during the corrosion of iron or steel in sodium chloride solution are presented in Figure 2. Most of the reactions at

the anode involve the release of hydrogen ions. If corrosion is localised and H^+ accumulates at the anodic corrosion sites, the local pH of these sites will be lower than the rest of the sample. Assuming that corrosion of iron occurs in the corrosion solution as described in section 2.1, the emission intensity of 56CF in the corrosion solution will be modulated by its local environment. If the emission intensity of 56CF in the proximity of the iron surface is monitored, localized corrosion sites will appear as dark spots and hence can be identified. The fluorescence intensity information can be directly correlated to the pH value using Figure 1d and thus the local concentration of hydrogen [H^+] can be calculated.

Corrosion of iron was conducted in a corrosion cell, shown schematically in Figure 2. A ground iron sample (the anode) and a transparent indium tin oxide (ITO) glass slide (the cathode) are separated by the corrosion solution. In this study a constant current of 100 μA was applied to the corrosion cell to accelerate the corrosion of iron. The real-time voltage and current were recorded by a DC voltage and current data logger (OMEGA UK).

The corrosion cell is placed on top of a home-built imaging set-up as shown in Figure 3 and illuminated by a 470 nm blue light-emitting diode (Thorlabs). This, based on the excitation spectrum in Figure 1a, is sufficient to excite 56CF so that the corrosion solution fluoresces. The intensity of the light-emitting diode (LED) was controlled by a programmable voltage source. To avoid photobleaching of 56CF, the LED was operated in triggered mode with the exposure time and the cycle time set at 70 ms and 125 ms respectively. Epi-fluorescence imaging was used to observe how fluorescence intensity changes with time. In all experiments, a 20× (N.A. = 0.5) Zeiss objective was used to observe the sample surface. Intensity images due to the 56CF emission were captured through the objective by a Falcon EMCCD camera. A 505 nm dichroic mirror, and a 495 nm long pass filter were used to ensure that only light emitted from 56CF was collected.

The intensity images obtained are analogues to pH maps. The sequence of intensity images captured during a corrosion experiment provides information on how local pH and hence corrosion of iron progresses with time. An image sequence consists of typically 720 images over a period of 90 seconds. To aid the identification of local corrosion sites, the following image normalisation process was carried out using ImageJ [36]. Each image in a sequence was first normalised by the average of the first four images to remove any visible features unrelated to 56CF emission and also fluorescence intensity from the bulk solution (which is assumed to be not affected by corrosion occurring on the surface). The average intensity of each image was then evaluated and the intensity of every pixel in the same image was then normalised by this average value. This results in an image in which pixels corresponding to uncorroded and corroded regions will have a I_N value of 1 and less than 1 respectively. The pH of these regions can then be obtained by Figure 1d. Each image consists of 502 × 501 pixels and each pixel corresponds to a spot of diameter 0.83 μm.

Raman spectroscopy was performed to examine any corrosion product on the iron sample immediately after corrosion experiments were conducted. This used a WITec Confocal Raman spectrometer alpha300 equipped with multiple objectives and a charge-coupled device (CCD) detector. A green Nd:YAG laser with 532 nm wavelength was employed as an excitation source and a 50× objective (NA 0.7) was used to collect Raman spectra. This results in a pixel size of 125 nm and a resolution of about 390 nm. The laser power was always kept low at approximately 1 mW to avoid sample degradation by laser heating. The accumulation time was 60 seconds. The corroded samples were rinsed gently with ethanol and blown dry with nitrogen before the Raman measurement.

3. Results and Discussion

3.1 Quantification of corrosion rate with changes in fluorescent intensity

Initially the smoothest iron surface, having *Ra* = 30.5±7.9 nm, was used as anode. It was immersed in 0.1 M NaCl solution in the presence of 50 μM 56CF (pH = 4.6) under an external constant DC current of 100 μA. Raw images and the corresponding normalised images, showing how the fluorescence intensity changes during an experiment, are shown in Figure 4a, and Figure 4b respectively. While it is difficult to distinguish any corrosion features in the raw images, the normalisation process outlined in Section 2 successfully highlights corrosion sites, which appear as dark spots against a white background. While spots may appear any time within the experimental time window, most of them, once they appear, stay until the end of the experiment. Only these spots are considered to be corrosion sites. In the experiment presented in Figure 4, the first clear dark spot with a diameter of 1.0 ~ 1.6 μm emerged at t = 0.75 s (not shown) and grew to a diameter ~ 4.1 μm at t = 45 s (spot 1, in Figure 4d). By t = 45 s, 27 dark spots had appeared in the imaging area; these dark spots are corrosion pits that have formed on the iron surface. Magnified images of a region highlighted (black rectangle) in Figure 4b for t = 10 s and t = 45 s are presented in Figures 4c and 4d. They show that these spots grew at different rate and were of various sizes and shapes. This suggests that the corrosion process is highly heterogeneous.

When a constant current of 100 μA was applied between the anode and cathode, the corresponding voltage was *ca* 0.70 V. At this voltage and the quite low pH ~ 4.6 of the corrosion solution, the Pourbaix diagram for iron [37,38] suggests that the final reaction products should be γ-FeOOH (see equation (7) in Figure 2). Therefore all the other six anode reactions listed in Figure 2 will be triggered, and hydrogen ions will be continuously released until these corrosion pits are passivated. As such, the pH and the fluorescence intensity emitted at these pits should drop as corrosion progress. The corrosion of each of five pits, circled (solid line circles) in Figure 4d, is monitored in Figure 5. A sixth dash line circle, labelled 'R' in Figure 4d, which represents a region that experienced no corrosion, is also included for reference. The normalised fluorescent intensity, I_N, at these five pits decreases while the intensity of

the reference point remains constant with time (Figure 5). The local I_N of all five pits dropped quickly from 1.00 to less than 0.90 during the first 15 s, with that of pits 3 and 5 dropping below 0.85 in the first 10 s. After 20 to 25 s, both I_N and the size of the pits stabilized (Figure 4b and inset A of Figure 5). The rapid decrease of I_N indicates that the decrease in local pH of these pits was correspondingly rapid. The subsequent levelling of I_N may be due to the pits being passivated by corrosion products such that an equilibrium is reached between the generation speed and the diffusion speed of the hydrogen ions in the pit areas.

The I_N in insert A, Figure 5 can be used to find the local pH in the pits using Figure 1d. The local hydrogen ion concentration can then be calculated by $[H^+] = 10^{-pH}$. Insert B in Figure 5 shows how local $[H^+]$ changes with time. It can be seen that the local $[H^+]$ in the corrosion pits roughly doubles compared to the bulk $[H^+]$ in the corrosion solution. The rate of hydrogen ions generation can be estimated by differentiating the concentration of hydrogen ion with time, as shown in Figure 5. The rate of hydrogen ion generation increases, reaches a maximum, and then reduces.

It is obvious from Figure 5 that each of the pits monitored was corroding at a different rate and to a different extent, with pits 1, 3 and 5 experiencing faster corrosion than pits 2 and 4. Overlaying fluorescence intensity image with topographic image of the same surface regions (Figure 6) reveals that all pits are located either at the edge of surface scratches or at the point of the intersection of two scratches. This suggests surface features may enhance the corrosion process; hence the effect of surface topography cannot be ignored.

Increasing the applied current to 175 μA (voltage ~1.0 V) increased the corrosion rate of iron (Figures 7 and 8), with the first dark spot now emerging at t = 2.6 s (not shown). The normalised images, Figure 7, taken during the corrosion process shows that dark spots are more distinguishable and larger than was the case with lower applied current (Figure 4). Five dark spots (solid line circles) and one reference spot (dash line circle labelled 'R') are circled in Figure 7b and the change in their local

hydrogen ion concentration with time is shown on Figure 8a. Over 60 pits were identified at t = 45 s, compared to only 27 when current was 100 μA. The normalised fluorescence intensity of pits 1 and 3 quickly decreased to below 0.85 at t = 10 s, and dropped further to around 0.80 at t = 20 s (not shown). Pit 1 had the lowest I_N of 0.76 at t = 45 second (not shown). This corresponds to a pH value of 4.16 and local $[H^+]$ of 6.87×10^{-5} M. Its size also grew from about 1 μm when it first emerged to ~ 8.3 μm at t = 45 s, which is twice the pit size seen at 100 μA (Figure 4c). The change in local $[H^+]$ for pits highlighted in Figure 7b is shown in Figure 8a. The final local $[H^+]$ for these pits is roughly 2 to 2.5 times that of bulk $[H^+]$. While the average final $[H^+]$ is higher, the initial corrosion progresses more slowly at 175 μA (Figure 8) than at 100 μA (Figure 5). At this higher applied current, pits also preferentially form on scratches and interaction points of scratches.

3.3 Roughness effects

Results in section 3.2 show that corrosion pits form adjacent to roughness features, hence surface topography can affect corrosion of iron in salt solutions. To verify the effect of surface topography, experiments were conducted using iron surfaces of three different roughnesses at 100 μA. For the iron sample that had been ground by 800 grit abrasive paper (medium roughness surface), dark spots started appearing at t = 48 s (spot 5), and only five dark spots were formed by t = 90 s (Figure 9). These spots (solid line circles) and also one reference spot (dash line circle, labelled 'R') are circled in Figure 9b and the time evolution of local $[H^+]$ and the rate of H^+ generation at these pits are presented in Figure 10. All pits developed more slowly and showed a relatively small change of $[H^+]$ in 90 s (Figure 10a), compared to results obtained with smooth iron surface (Figure 5). The maximum $[H^+]$ and maximum rate of H^+ generation were 3.96×10^{-5} M and 1.9×10^{-6} mol/(L·s) respectively for medium roughness surface.

The roughest sample, produced by grinding with 400 grit abrasive paper, showed even slower corrosion. Only two corrosion pits were seen after 90 s (not shown). The drop in I_N in this case was similar to the results obtained with medium roughness surface, with a maximum local $[H^+]$ of 3.99×10^{-5} M and a maximum rate of H^+ generation of 7.37×10^{-7} Mol/(L·s). Hence the change of abrasive paper from 800 grit to 400 grit seems to affect the number of corrosion pits on the iron surface rather than the rate at which corrosion progresses at these pits.

The number of corrosion pits formed in 90 s for three samples ground with the various abrasive papers are summarised in Figure 11. Data were collected from at least 3 samples of each surface roughness. Three zones can clearly be identified corresponding to the 3 different roughnesses. In all cases, the number of corrosion pits increases with time and then plateaus, although pits form at a higher rate for smoother samples. Smooth samples formed significantly more pits than the other samples even in the first 10 seconds. For the roughest surface, none of the samples produced more than three pits within 90 s.

The observation that a smoother surface gives rise to more corrosion pits may seem counter-intuitive and is believed to be a result of the implementation of constant current experiments. Note that the *Ra* values for samples prepared with 4000, 800, and 400 grit abrasive paper are 30.5±7.9 nm, 266.3±13.7 nm and 505.8±53.8 nm respectively. While the apparent area in contact with the corrosion medium is the same for all samples, the real area of contact increases with surface roughness. Since constant current was applied in this study, an increase in real area with increasing roughness means the rougher the surface, a lower the actual current density. This could lead to the reduction in pit formation rate observed in this study. This observation highlights that care must be taken when interpreting results obtained from accelerated corrosion tests. Having said that, this study shows that surface features have a significant effect on the initiation of corrosion, with corrosion pits appearing in proximity to scratches in all samples.

3.4 Characterisation of corrosion products

The iron samples were cleaned and observed with an optical microscope before and immediately after the corrosion experiments. Their surface topography was also recorded before and at the end of each test. No corrosion-induced surface topography changes were observed after 90 s tests (not shown). This is probably because, although the fluorescence technique is capable of detecting changes in pH in single molecule level, it is also diffraction-limited. This means that any object that is smaller than half of the wavelength of excitation light, λ, will be portrayed as an object of size of $\frac{\lambda}{2}$. Since a 470 nm LED was used as the excitation source in this experiment, any pit smaller than 200 nm in size will be seen as at least 235 nm. In the corrosion experiments conducted, the diffusion of $[H^+]$ in the solution will also make the pits appear larger. Hence pits observed with fluorescence imaging might not be readily detected by other technique that measure changes in surface topography. This highlights that the developed technique is ideal for monitoring early stage corrosion that would otherwise be missed by other techniques.

Raman spectroscopy was applied to characterise corrosion products, if any, on iron surfaces. Iron samples were examined with Raman spectroscopy after corrosion in 0.1 M NaCl aqueous solution at a constant current 100 μA for both of 1 minute and 5 minutes. No 56CF was used in these experiments since fluorescence from 56CF may overwhelm the relatively weak Raman signals. Instead, the pH of the solution was adjusted with acetic acid to 4.6. Two challenges were encountered. It is likely that only a very small amount of corrosion products would be generated within the experimental window of 45 s. With hardly any corrosion-induced topographical changes or discolouring at such a short exposure, the location of pits on the iron surface is difficult. Indeed without the help of 56CF, corrosion pits can hardly be identified after 1 minute of corrosion with white light illumination. Hence the sampling size is small. Secondly, the local corrosion of iron is heterogeneous (see

Figures 5, 8 and 10). Thus any Raman spectra obtained are likely biased towards pits that are at more advanced stage of corrosion. With these limitations in mind, the results on Raman spectra were obtained from these iron samples. Individual Raman spectra were obtained from each pixel across the whole exposed surface and used to identify locations where corrosion had occurred. These locations were presumed to correspond to corrosion pits although only rarely could the actual pits be identified optically.

For a smooth surface that was exposed to the corrosion medium for one minute, only very few spectral features resembling those of iron corrosion products were obtained. Two of these are shown in Figure 12a. For pit_1, strong characteristic bands at 225, 291, 409 and 498 cm^{-1} were observed. For pit_2, characteristic bands at 214 and 273 cm^{-1} were obtained. These spectra were assigned to two different form of α-Fe_2O_3 (see equation (8) in Figure 2) [39,40]. Raman spectra of the regions surrounding these sites, and from all other regions were similar to spectrum of freshly ground iron sample (not shown).

After the smooth iron sample has been exposed to the corrosion medium for 5 minutes, corrosion pits could easily be identified both using Raman spectra and by eye. Some of these were surrounded by regions of brown rust. Typical Raman spectra from these pits are shown in Figure 12c. The spectrum for pit_3 (5 min) is similar to that of pit_2 in Figure 12a (1 min) but with much stronger Raman signals. On the other hand, even though the spectrum of pit_4 (5 min) is similar to that of pit_1 of Figure 12a (1 min), its intensity is very weak. This suggests the α-Fe_2O_3 with characteristic bands at 214, 275, 390 and 584 cm^{-1} is more prominent in corrosion pits as corrosion progresses. From the brown rust surrounding the corrosion pits, the characteristic bands at 249 and 378 cm^{-1} were observed (see Figure 12c). This suggests that these brown rust is γ-FeOOH [41,42], which is a stable reaction product in this condition,

For medium roughness surface, only one possible pit position showed some Raman signal, as indicated in Figure 12b. For pit_5, two small characteristic bands at 225 and 291 cm^{-1}, assigned to α-Fe_2O_3, were observed. This is the same as for Pit_1 on the smooth sample, as shown in Figure 12a. Again no Raman signal was observed for the regions surrounding the corrosion pits and far from the pit. More pits were obtained after 5 minutes of corrosion. However the number of pits observed was much fewer than that with the smooth surface. Raman spectra corresponding to both forms of α-Fe_2O_3 were obtained (see pit_7 and pit_8 in Figure 12d). For those areas around and far the pits, no Raman spectrum for corrosion products could be identified. Compared to the Raman results from smooth sample corroded for the same time, the rougher surface clearly has less corrosion than the smooth one. This confirms our results obtained with epi-fluorescence imaging.

4. Conclusion

A versatile method has been developed to detect the initial-stage of the iron corrosion *in-situ* using a pH-sensitive fluorescent dye. A decreased fluorescence intensity inside corrosion pits is induced by continuous release of hydrogen ions as a product of iron corrosion. The concentration of hydrogen ions can thus be monitored and quantified in real-time by measuring the localized fluorescence intensity of pits. This method allows identification of individual corrosion pits and quantification of corrosion rate. The method has a spatial resolution of < 1 μm and in principle can detect pH change to single molecular level. Its high sensitivity means that local information on iron corrosion can be obtained in real time with minimum external perturbation. The ability of the technique to pick up early signs of corrosion in a very short time frame also leads to potential application to material selection and investigation of slow progressing corrosion. The developed technique was applied to investigate the effect of surface roughness on corrosion rate of iron. It was found that surface scratches promote the formation of corrosion pits. Hence surface features govern the initiation and location of corrosion sites. The study also shows that

surface roughness, under a constant current condition, influences the corrosion of iron primarily by affecting number of corrosion pits on the surface. The smoother the surface, the more pits formed due to increased current density.

Acknowledgement

This study was supported by EPSRC Platform Grant (EP/G026114/1), EPSRC Grant EP/J015385/1. The authors would like to thank Mourad Chennaoui for help in the design of the experiments.

References

[1] W. Li, D.Y. Li, In situ measurements of simultaneous electronic behavior of Cu and Al induced by mechanical deformation, J. Appl. Phys., 99 (2006)073502-073508.
[2] V.V. Levitin, O.L. Garin, V.K. Yatsenko, S.V. Loskutov, On structural sensibility of work function, Vacuum, 63 (2001) 367-370.
[3] G.L. Song, D. Haddad, The topography of magnetron sputter-deposited Mg-Ti alloy thin films, Mater. Chem. Phys., 125 (2011) 548-552.
[4] M.S. Xue, J. Xie, W. Li, C.G. Yang, Y.L. Ai, F.J. Wang, J.F. Ou, J.P. Yao, Dependence of electron work function of Al-Mg alloys on surface structures and relative humidity, Physica. B, 406 (2011) 4240-4244.
[5] W. Li, D.Y. Li, Influence of surface morphology on corrosion and electronic behavior, Acta Mater., 54 (2006) 445-452.
[6] Y. Zhou, J.Q. Lu, W.G. Qin, Change in the electronic work function under different loading conditions, Mater. Chem. Phys., 118 (2009) 12-14.
[7] K. Sasaki, G.T. Burstein, The generation of surface roughness during slurry erosion-corrosion and its effect on the pitting potential, Corros. Sci., 38 (1996) 2111-2120.
[8] T. Hong, M. Nagumo, Effect of surface roughness on early stages of pitting corrosion of type 301 stainless steel, Corros. Sci., 39 (1997) 1665-1672.
[9] L.R. Hilbert, D. Bagge-Ravn, J. Kold, L. Gram, Influence of surface roughness of stainless steel on microbial adhesion and corrosion resistance, Int. Biodeter. Biodegr., 52 (2003) 175-185.
[10] G.T. Burstein, P.C. Pistorius, Surface-Roughness and the Metastable Pitting of Stainless-Steel in Chloride Solutions, Corrosion, 51 (1995) 380-385.
[11] S.K. Kim, I.J. Park, D.Y. Lee, J.G. Kim, Influence of surface roughness on the electrochemical behavior of carbon steel, J. Appl. Electrochem., 43 (2013) 507-514.
[12] L. Abosrra, A.F. Ashour, S.C. Mitchell, M. Youseffi, Corrosion of mild steel and 316L austenitic stainless steel with different surface roughness in sodium chloride saline solutions, in: C.A. Brebbia, R.A. Adey (Eds.) Electrochemical Process Simulation Iii, 2009, pp. 161-172.
[13] H.H. Huang, Variation in corrosion resistance of nickel-titanium wires from different manufacturers, Angle Orthod., 75 (2005) 661-665.

[14] T.H. Lee, T.K. Huang, S.Y. Lin, L.K. Chen, M.Y. Chou, H.H. Huang, Corrosion resistance of different nickel-titanium archwires in acidic fluoride-containing artificial a aliva, Angle Orthod., 80 (2010) 547-553.
[15] R.M. Pidaparti, R.K. Patel, Investigation of a single pit/defect evolution during the corrosion process, Corros. Sci., 52 (2010) 3150-3153.
[16] Y. Tan, Sensing localised corrosion by means of electrochemical noise detection and analysis, Sens. Actuators, B, 139 (2009) 688-698.
[17] D.H. Xia, S.Z. Song, J.H. Wang, J.B. Shi, H.C. Bi, Z.M. Gao, Determination of corrosion types from electrochemical noise by phase space reconstruction theory, Electrochem. Commun., 15 (2012) 88-92.
[18] J. Xu, X.J. Wu, C. Cheng, A.R. Ben, A Magnetic Flux Leakage and Magnetostrictive Guided Wave Hybrid Transducer for Detecting Bridge Cables, Sensors-Basel, 12 (2012) 518-533.
[19] G. Du, J. Li, W.K. Wang, C. Jiang, S.Z. Song, Detection and characterization of stress-corrosion cracking on 304 stainless steel by electrochemical noise and acoustic emission techniques, Corros. Sci., 53 (2011) 2918-2926.
[20] N.R. Cawley, D.G. Harlow, Spatial statistics of particles and corrosion pits in 2024-T3 aluminium alloy, J. Mater. Sci., 31 (1996) 5127-5134.
[21] C.H. Paik, H.S. White, R.C. Alkire, Scanning electrochemical microscopy detection of dissolved sulfur species from inclusions in stainless steel, J. Electrochem. Soc., 147 (2000) 4120-4124.
[22] M. Buchler, J. Kerimo, F. Guillaume, W.H. Smyrl, Fluorescence and near-field scanning optical microscopy for investigating initiation of localized corrosion of Al 2024, J. Electrochem. Soc., 147 (2000) 3691-3699.
[23] M.A. Alodan, W.H. Smyrl, Detection of localized corrosion of aluminum alloys using fluorescence microscopy, J. Electrochem. Soc., 145 (1998) 1571-1577.
[24] M. Buchler, T. Watari, W.H. Smyrl, Investigation of the initiation of localized corrosion on aluminum alloys by using fluorescence microscopy, Corros. Sci., 42 (2000) 1661-1668.
[25] P. Schmutz, G.S. Frankel, Corrosion study of AA2024-T3 by scanning Kelvin probe force microscopy and in situ atomic force microscopy scratching, J. Electrochem. Soc., 145 (1998) 2295-2306.
[26] K. Kowal, J. DeLuccia, J.Y. Josefowicz, C. Laird, G.C. Farrington, In situ atomic force microscopy observations of the corrosion behavior of aluminum-copper alloys, J. Electrochem. Soc., 143 (1996) 2471-2481.
[27] R.M. Rynders, C.H. Paik, R. Ke, R.C. Alkire, Use of in-situ atomic-force microscopy to image corrosion at inclusions, J. Electrochem. Soc., 141 (1994) 1439-1445.
[28] M.L. Patterson, C.S. Allen, Fluorescence detection of polishing alumina on glassy-carbon electrode surfaces, Anal. Chem., 57 (1985) 2751-2752.
[29] R.C. Engstrom, S. Ghaffari, H.W. Qu, Fluorescence imaging of electrode solution interfacial processes, Anal. Chem., 64 (1992) 2525-2529.
[30] S. Szunerits, D.R. Walt, Aluminum surface corrosion and the mechanism of inhibitors using pH and metal ion selective imaging fiber bundles, Anal. Chem., 74 (2002) 886-894.
[31] A. Augustyniak, J. Tsavalas, W. Ming, Early detection of steel corrosion via "turn-on" fluorescence in smart epoxy coatings, ACS Appl. Mater. Interfaces, 1 (2009) 2618-2623.

[32] R.M. Pidaparti, E.B. Neblett, S.A. Miller, J.C. Alvarez, Monitoring the corrosion process of Al alloys through pH induced fluorescence, Smart Mater. Struct., 17 (2008) 015001.
[33]A.A. Panova, P. Pantano, D.R. Walt, In situ fluorescence imaging of localized corrosion with a pH-sensitive imaging fiber, Anal. Chem., 69 (1997) 1635-1641.
[34]A. Augustyniak, W. Ming, Early detection of aluminum corrosion via “turn-on” fluorescence in smart coatings, Prog. Org. Coat., 71 (2011) 406-412.
[35]W.T. Liu, J.H. Wu, E.S.Y. Li, E.S. Selamat, Emission characteristics of fluorescent labels with respect to temperature changes and subsequent effects on DNA microchip studies, Appl. Environ. Microb., 71 (2005) 6453-6457
[36] T.J. Collins, ImageJ for microscopy, Biotechniques, 43 (2007) 25-30.
[37] P. Refait, J.M.R. Genin, The oxidation of ferrous hydroxide in chloride-containing aqueous-media and Pourbaix diagrams of green rust one, Corros. Sci., 34 (1993) 797-819.
[38] P. Sarin, V.L. Snoeyink, D.A. Lytle, W.M. Kriven, Iron corrosion scales: Model for scale growth, iron release, and colored water formation, J. Environ. Eng-Asce, 130 (2004) 364-373.
[39] A.M. Martin, K. Righter, Melting of clinopyroxene plus magnesite in iron-bearing planetary mantles and implications for the Earth and Mars, Contrib Mineral Petr, 166 (2013) 1067-1098.
[40]D.L.A. deFaria, S.V. Silva, M.T. deOliveira, Raman microspectroscopy of some iron oxides and oxyhydroxides, J. Raman Spectrosc., 28 (1997) 873-878.
[41]S.X. Li, L.H. Hihara, In situ Raman spectroscopic study of NaCl particle-induced marine atmospheric corrosion of Carbon Steel, J. Electrochem. Soc., 159 (2012) C147-C154.
[42] S.X. Li, L.H. Hihara, In situ Raman spectroscopic identification of rust formation in Evans' droplet experiments, Electrochem. Commun., 18 (2012) 48-50.

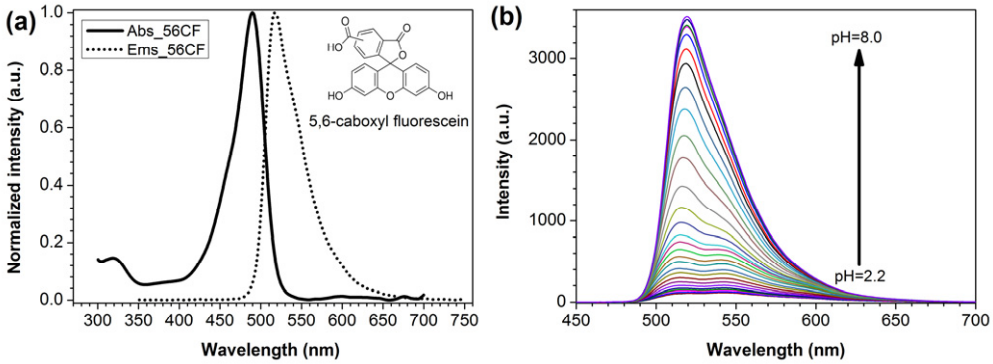

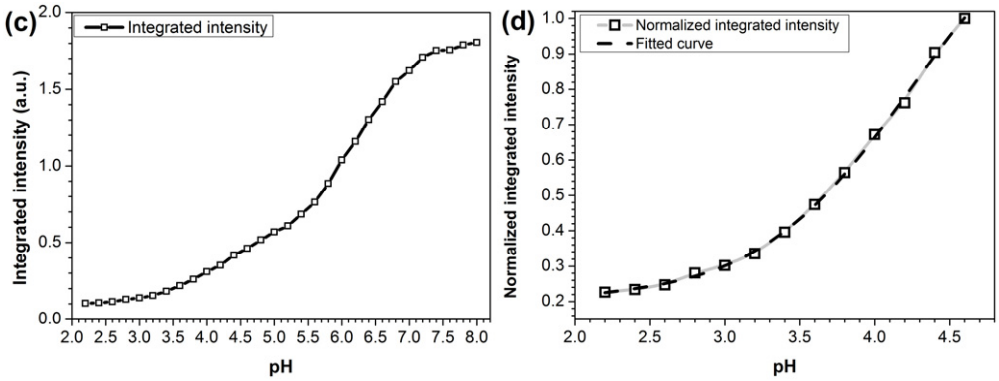

Figure 1 (a) Adsorption and emission spectra of 10 μM 56CF in pH 7 buffer; (b) emission spectra of 10 μM 56CF in buffer solutions with different pH; they were measured with buffers of pH varying in an increment of 0.2; (c) integrated emission intensity as a function of pH (integration range: 495 nm – 750 nm); (d) normalized integrated emission intensity from pH=2.2 to pH=4.6.

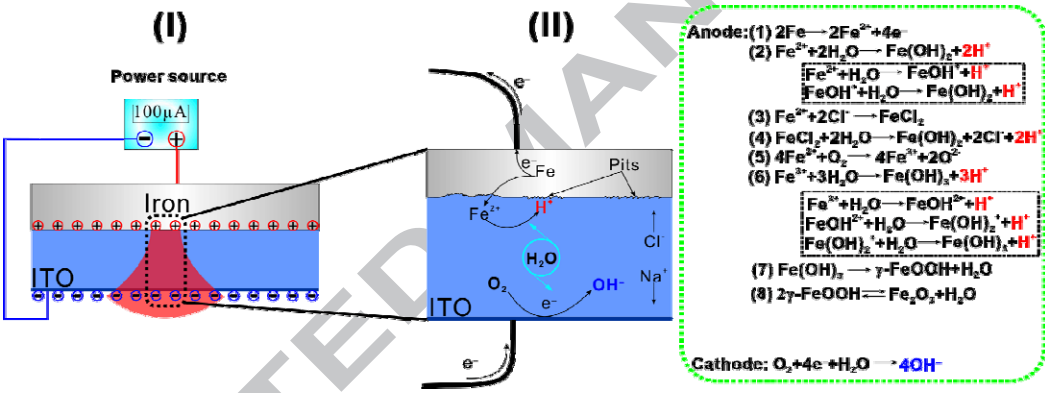

Figure 2. Possible reactions at anode (iron) and cathode (ITO glass) during corrosion of iron in NaCl solution.

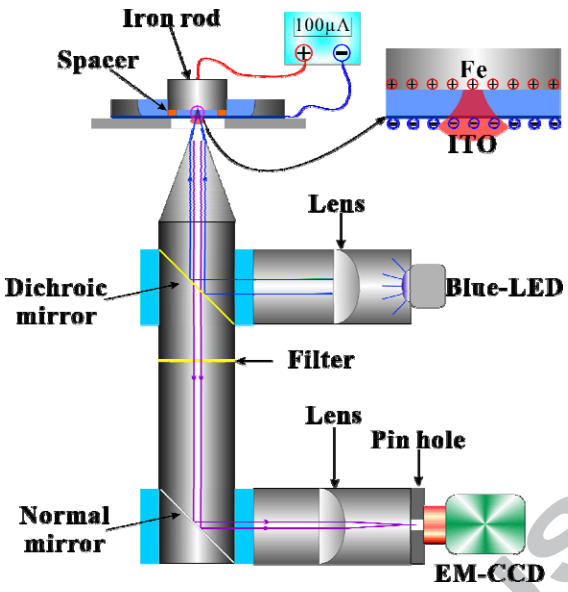

Figure 3 A schematic of the home-built epi-fluorescence imaging setup used to monitor the corrosion of iron in a corrosion cell.

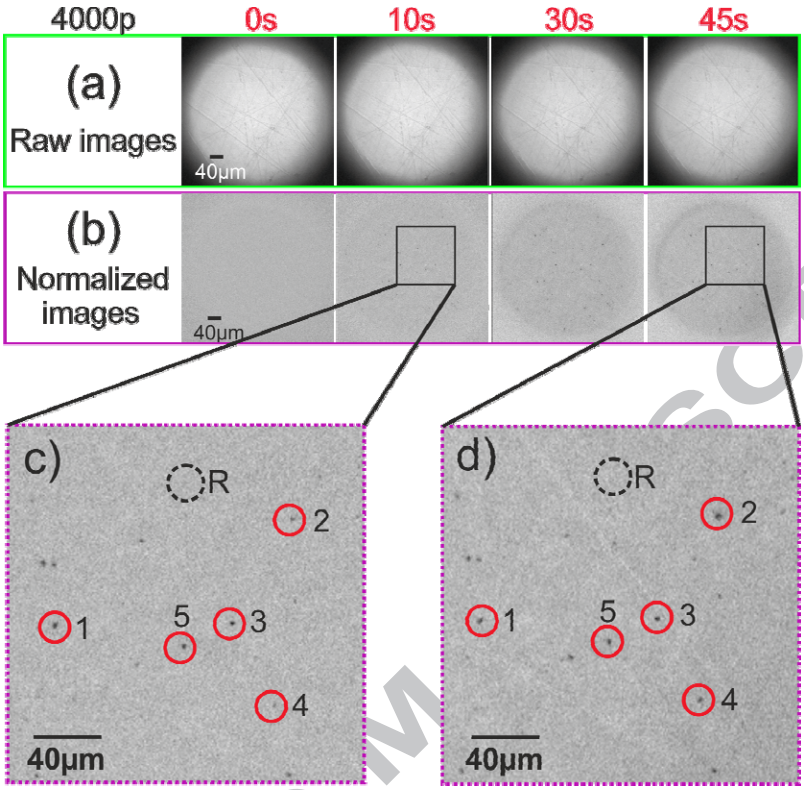

Figure 4 *In situ* fluorescence images of 4000 grit abrasive paper ground iron under 100 μA in 45 s (a) raw images, and (b) corresponding normalized images. (c) Magnified image at t =10 s; and (d) magnified image at t = 45 s. Five dark spots are marked with solid line circles and one reference spot is marked with a dash line circle.

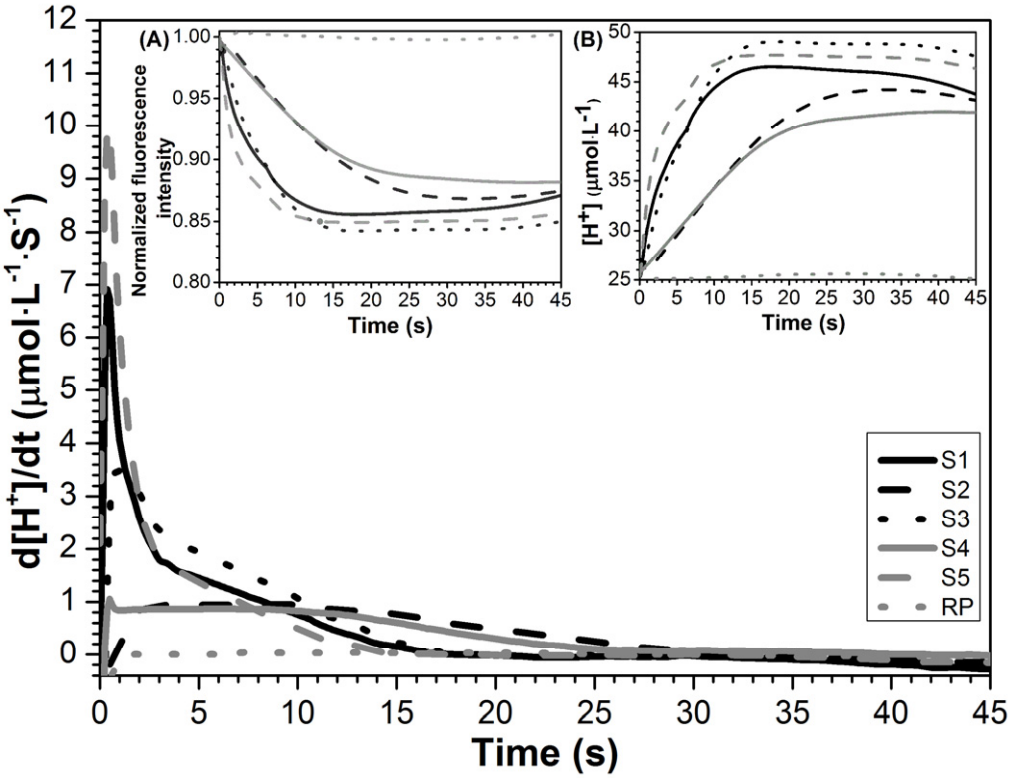

Figure 5 The rate of H^+ generation as a function of time of 5 circled pits on Figure 4d (at 100 μA). The inserts are (A) normalised fluorescence intensity changes with time; and (B) the corresponding changes of localized concentration of H^+ respectively.

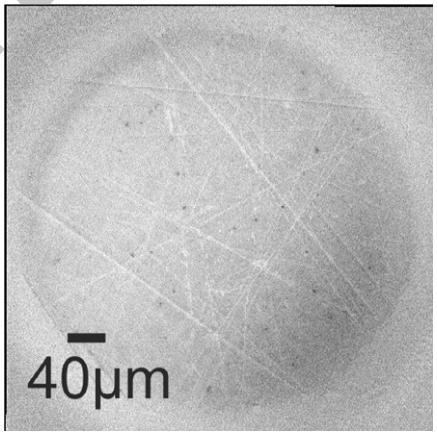

Figure 6 *In situ* fluorescence images of 4000 grit abrasive paper ground iron under 100 μA in 90 s. The dark spots are corrosion pits and white lines are surface scratches produced by the grinding process.

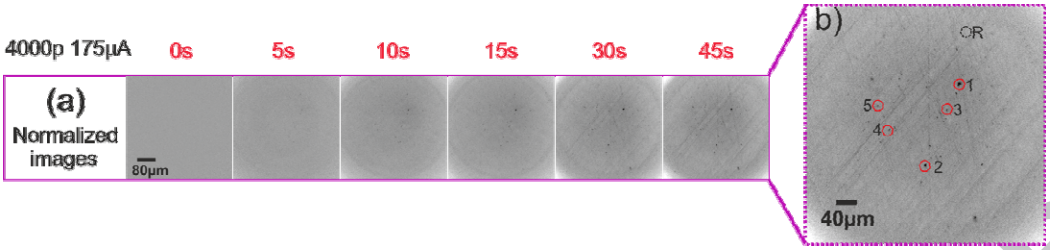

Figure 7 (a) *In situ* normalised fluorescence images of 4000 grit-ground iron under 175 μA in 45 s. (b) The frame taken at 45th s is marked with five dark spots (solid line circles) and one reference spot (dash line circle, labelled 'R').

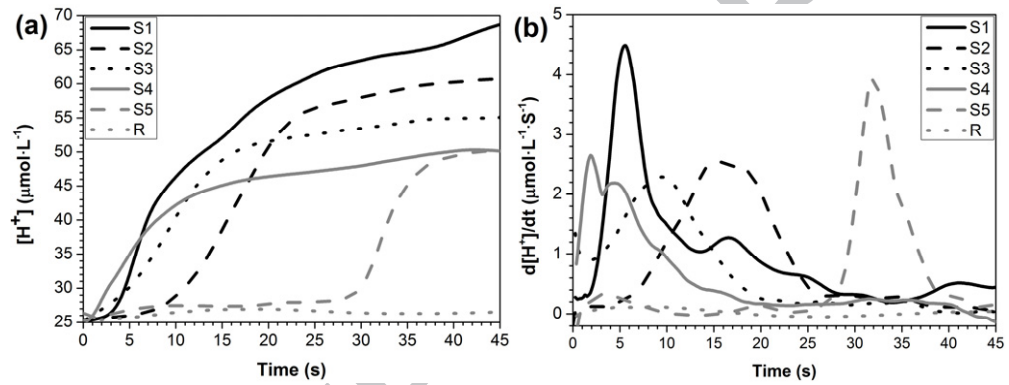

Figure 8 (a) The localized concentration of H^+ based on fluorescence intensity change of six marked spots in Figure 7b (at 175 μA). (b) The H^+ generation rate as a function of time.

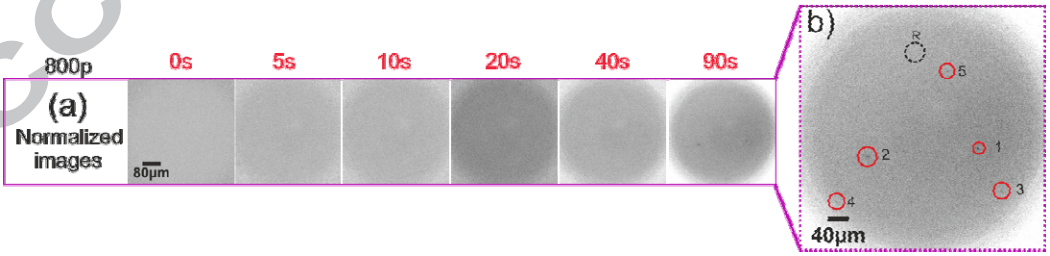

Figure 9 (a) *In situ* normalised fluorescence images of 800 grit-ground iron under 100 μA in 90 s. (b) The frame taken at t = 45 s marked with five dark spots (solid line circles) and one reference spot (dash line circle, labelled 'R').

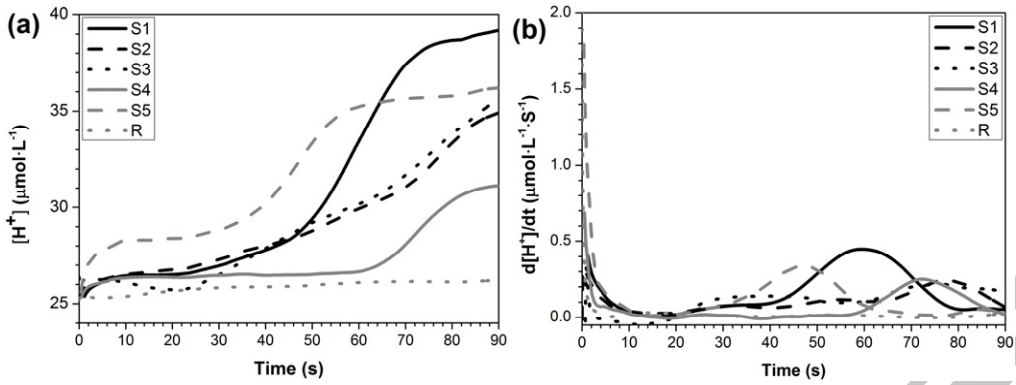

Figure 10 (a) The localized concentration of H^+ based on normalised fluorescence intensity change of six marked spots in Figure 9(b) (at 100 μA). (b) The H^+ generation rate as a function of time.

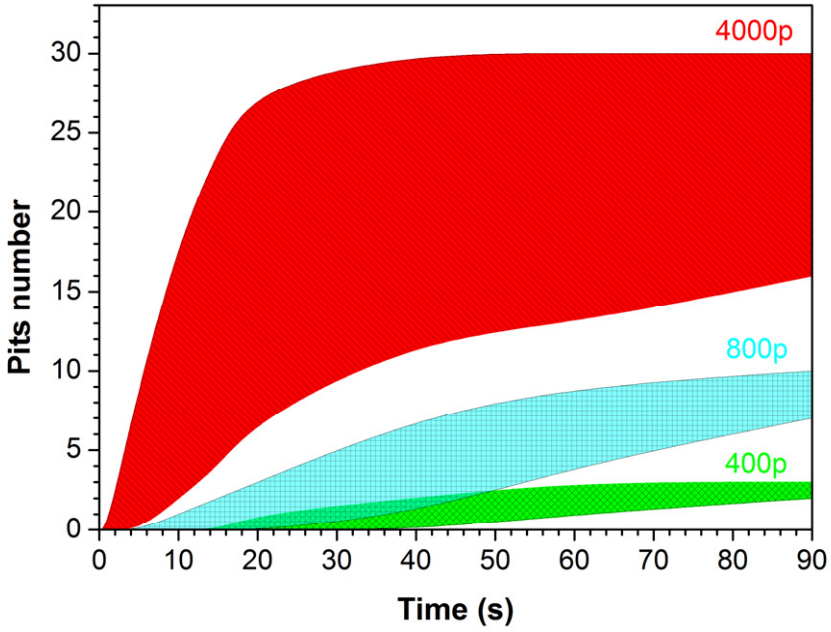

Figure 11 Statistical analysis of corrosion pit number as a function of time.

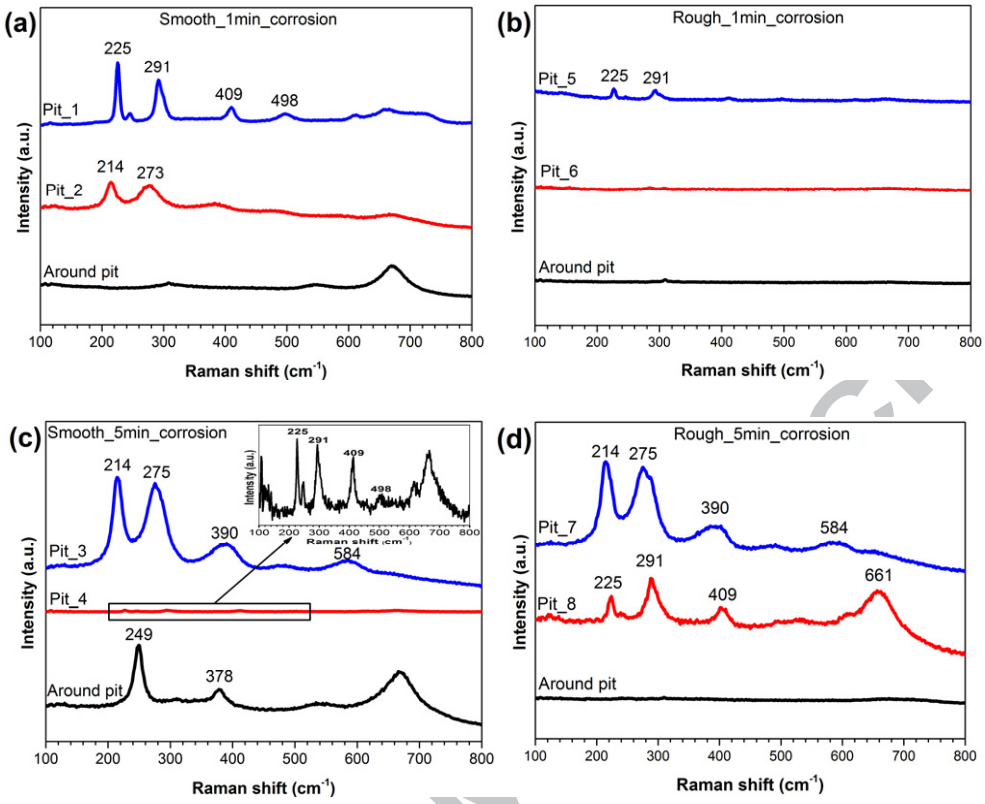

Figure 12 Raman spectra from different locations on the iron in 0.1M NaCl solution with pH=4.60 (tuned by 0.01M acetic acid): (a) 4000 grit abrasive paper ground iron and (b) 1200 grit ground iron after 1 min corrosion (100 μA). (c) 4000 grit ground iron and (d) 1200 grit ground iron after 5 min corrosion (100 μA).

Highlights

- Fluorescence imaging based corrosion detection method was developed.
- Time and spatial resolutions of 125 ms and <1 μm respectively were achieved.
- Incipient corrosion pits on iron surfaces in salt solutions were observed.
- Corrosion pits preferentially forms along surface features such as scratches.